Acoustic Loss in Thin-Film Lithium Niobate: An Experimental Study

Ruochen Lu, *Member, IEEE*, Yansong Yang, *Member, IEEE*, and Songbin Gong, *Senior Member, IEEE*

***Abstract*— This work reports an experimental study of acoustic loss in thin-film lithium niobate ($LiNbO_3$) using acoustic delay lines (ADLs). Unlike prior resonator-based quality factor (Q) studies, this approach directly extracts the damping in thin-film $LiNbO_3$, avoiding the influence of other intricate loss mechanisms, e.g., anchor loss and electrode-induced loss. Acoustic attenuation of fundamental symmetric (S0) and shear horizontal (SH0) waves are studied in suspended $LiNbO_3$ thin films of different thicknesses. The attenuation is significantly higher in thinner $LiNbO_3$ films, suggesting the $LiNbO_3$ crystal degradation during the microfabrication as the primary loss origin. Nevertheless, the extracted equivalent Q in thin-film $LiNbO_3$ is still higher than reported values, suggesting that anchor design and electrode quality remain the bottlenecks for higher Q. The proposed loss extraction framework is readily extendable to other acoustic thin-film structures. [2021-0107]**

***Index Terms*— Acoustic attenuation, acoustic delay line, lithium niobate, piezoelectric resonators, quality factor, thin-film devices.**

I. Introduction

THIN-FILM lithium niobate ($LiNbO_3$) based acoustic microsystems have been extensively studied in the last decade, ranging from acoustic resonators [1]–[6], transformers [7]–[9], delay lines [10]–[14], to emerging acousto-electric amplifiers [15], non-reciprocal networks [16], [17], acousto-optic modulators [18]–[21], and quantum systems [22]. The platform receives growing research attention because various acoustic modes with high electromechanical coupling (K^2) and low loss can be excited in thin-film $LiNbO_3$. As a result, it enables efficient piezoelectric transduction between the electrical and acoustic domains. These modes, e.g., fundamental symmetric (S0) [6], shear-horizontal (SH0) [2], and first-order antisymmetric (A1) [1], which could not be efficiently excited in conventional bulk $LiNbO_3$ substrates [23], are only made available thanks to the thin-film transfer techniques of single-crystal $LiNbO_3$ [24], [25]. Up to now, thin-film $LiNbO_3$ devices have been demonstrated from a few MHz [26] to 60 GHz [27]. However, the presented performance is still far from the performance limits of bulk $LiNbO_3$ [28], resulting from the orders of magnitude higher acoustic wave attenuation observed in thin-film $LiNbO_3$ [10]–[14].

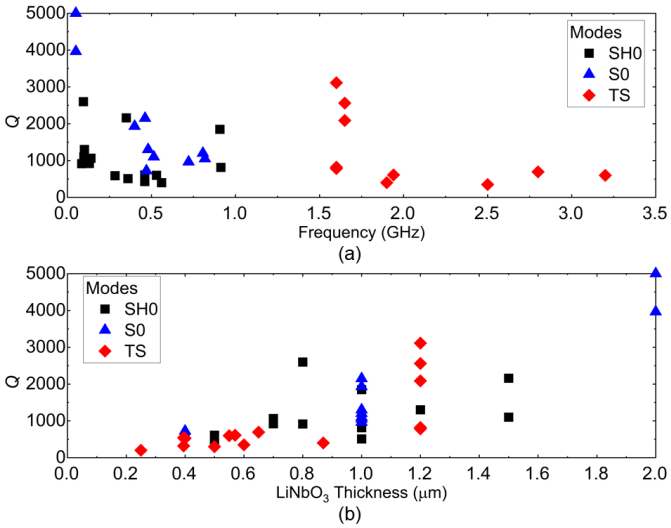

Fig. 1. Survey of the reported thin-film $LiNbO_3$ acoustic resonators with different (a) operating frequencies and (b) $LiNbO_3$ thicknesses.

To further advance low-loss thin-film $LiNbO_3$ technologies, one must first identify and mitigate the dominant loss mechanism. Conventionally, the acoustic loss in suspended microelectromechanical systems (MEMS) devices is primarily studied by analyzing the maximum achievable quality factor (Q) in resonators [29]–[31]. A survey of thin-film $LiNbO_3$ resonator Q is presented in Fig. 1, sorted by the operating frequency [Fig. 1 (a)] and $LiNbO_3$ thickness [Fig. 1 (b)]. It includes SH0 [2], [5], [32]–[38], S0 [4]–[6], [39]–[41], and thickness-shear (comprising A1) mode devices [1], [3], [42]–[48] with high K^2. Despite different designs and implementations, resonators at lower frequencies and using thicker $LiNbO_3$ tend to show higher Q. To further decipher the loss in thin-film $LiNbO_3$, especially to identify whether the thickness or frequency is the limiting factor, a similar Q-analysis using resonators with controlled lateral and thickness dimensions could be explored [29]. However, several issues persist. First, the anchor loss, which is highly sensitive to the resonator configuration [29], is hard to be controlled between resonators in different stack thicknesses or at different frequencies. Second, resonator Qs reflect the compound loss in both $LiNbO_3$ and electrodes, and it is hard to isolate

Manuscript received May 17, 2021; revised June 10, 2021; accepted June 23, 2021. Date of publication July 1, 2021; date of current version July 30, 2021. Subject Editor S. Tanaka. *(Corresponding author: Ruochen Lu.)*

Ruochen Lu is with the Department of Electrical and Computer Engineering, The University of Texas at Austin, Austin, TX 78712 USA (e-mail: ruochen@utexas.edu).

Yansong Yang and Songbin Gong are with the Department of Electrical and Computer Engineering, University of Illinois at Urbana–Champaign, Urbana, IL 61801 USA.

Color versions of one or more figures in this article are available at https://doi.org/10.1109/JMEMS.2021.3092724.

Digital Object Identifier 10.1109/JMEMS.2021.3092724

TABLE I
KEY DESIGN PARAMETERS

Sym.	Parameter	Value	Sym.	Parameter	Value
Λ	Cell length (μm)	3.2 – 7.44	W_A	Aperture width (μm)	120
L_G	Gap length (μm)	100 – 1200	t_{LN}	$LiNbO_3$ thickness (nm)	400 – 1600
N_c	Cell number	10	t_{Al}	Electrode thickness (nm)	120

and measure their contributions individually. Third, such a Q study suffers from the fabrication variation. A new loss characterization approach is needed to overcome these three bottlenecks.

To this end, recently developed unidirectional acoustic delay lines (ADLs) in thin-film $LiNbO_3$ could be a promising testbed [10]–[14]. Such ADLs are two-port devices with acoustic waves propagation between ports. First, in such ADLs, waves are predominantly confined between the unidirectional transducers on the opposite ends of the $LiNbO_3$ waveguide, eliminating the anchor loss concern. Second, the loss in metallic electrodes can be removed by analyzing ADLs with identical transducers but different waveguide lengths. Third, the fabrication variation could be mitigated by studying multiple ADLs with incremental waveguide lengths. The proposed loss extraction framework is readily extendable to other acoustic modes and thin-film structures at RF.

In this work, we report an experimental study of acoustic loss in thin-film $LiNbO_3$ using ADLs. Acoustic attenuation of S0 and SH0 waves are studied in X-cut $LiNbO_3$ of different thicknesses (400, 800, and 1600 nm). Loss is much higher in thinner $LiNbO_3$ films, suggesting crystal damage during the microfabrication as the limiting factor. Nevertheless, the extracted Q is higher than those reported in resonators, suggesting more room for improvement in resonator configuration and electrode optimization. The paper is organized as follows. Section II introduces the ADL design and loss extraction approach. Section III shows the fabricated device and material analysis. Section IV includes the measurement and discussion. Section V is the conclusion.

II. DESIGN AND SIMULATION

A. Acoustic Delay Line Testbed

The proposed ADL testbed schematic is presented in Fig. 2 (a), with key parameters listed in Table I. The device consists of 120 nm patterned interdigitated aluminum (Al) electrodes on the top of suspended single-crystal $LiNbO_3$ with thicknesses of 400, 800, and 1600 nm. A pair of unidirectional transducers are placed on the opposite ends of the $LiNbO_3$ acoustic waveguide (gap length L_G). The transducers follow the unidirectional design [49]. Each cell (length of Λ) includes a pair of $\Lambda/8$ non-reflective electrodes and a $3\Lambda/8$ distributed reflector [Fig. 2 (b)]. The electrodes' asymmetric arrangement within a cell leads to different phase delays for the waves reflected by adjacent reflectors, causing constructive (destructive) wave interference in the forward (backward) directions. With adequate cascaded cells (cell number N_c), unidirectional transducers can be achieved.

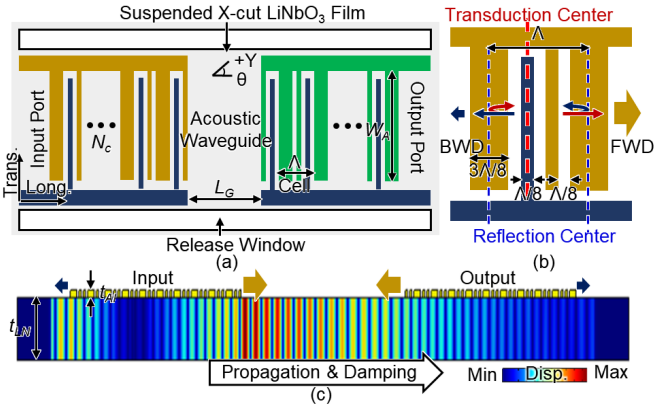

Fig. 2. (a) Mock-up view (top) of unireictional ADLs in thin-film $LiNbO_3$. (b) Transducer cell design. (c) Cross-sectional view of the simulated displacement modeshpe (film thickness and damping exaggerated).

The finite element analysis (FEA) simulated displacement mode shape of the ADL testbed is presented in Fig. 1 (c). In operation, incident electromagnetic (EM) signals are converted into acoustic vibration through piezoelectricity at the input transducer. Thanks to the unidirectional transducer, most energy is launched toward the output port, transversing the acoustic waveguide before converting it to EM signals. The received wave amplitudes differ in ADLs with different gap lengths (L_G) from the acoustic attenuation [exaggerated in Fig. 1 (c)]. The difference in amplitude will be used to extract the propagation loss (PL) in thin-film $LiNbO_3$. The unidirectional ADL design is crucial here to prevent forming a standing wave between ports, leading to severe in-band ripples, detrimental for the loss extraction.

B. SH0 and S0 Waves in Thin-Film $LiNbO_3$

This paper focuses on SH0 and S0 because their frequencies are primarily determined by lateral wavelength (λ), allowing for isolating the effects of $LiNbO_3$ thickness from the operating frequency. The damping of other acoustic modes (e.g., A1) will likely follow a similar trend but will not be investigated here.

X-cut $LiNbO_3$ is selected as the platform since both SH0 and S0 can be efficiently excited along the $-10°$ [12] and 30° [11] to +Y axis, respectively [50]. Three-dimension (3D) FEA eigenmode analysis (Fig. 2) is first performed for obtaining the dispersion of S0 and SH0 in 400, 800, and 1600 nm thick $LiNbO_3$. λ is set between 3 and 8 μm for GHz operation. In the simulation, electrical and mechanical periodic boundary conditions are applied to longitudinal and transverse direction edges. Mechanically free boundary conditions are applied to the top and bottom surfaces. The electrically open boundary condition is applied to the bottom, and the electrically open (short) is applied to the top for computing the frequencies f_o (f_s).

The simulated dispersion of SH0 and S0 are plotted in Fig. 3 (a) and (c), along with the displacement mode shapes. Both f_o and f_s are predominantly set by λ, and f_s has a weak dependency on the film thickness. f_o is larger than f_s due to the piezoelectric stiffening effect [23]. Note that S0 mode in 1600 nm thick X-cut $LiNbO_3$ with λ less than 5.5 μm

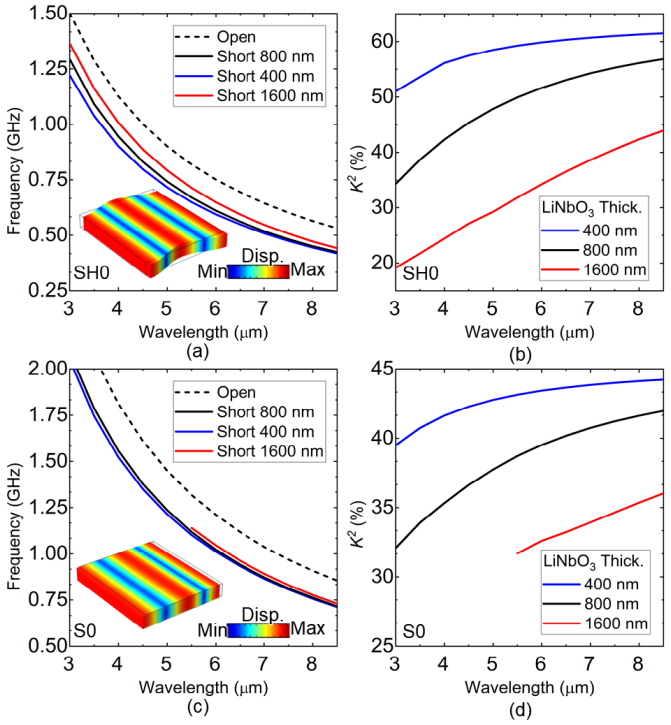

Fig. 3. Dispersion of GHz S0 and SH0 waves in X-cut $LiNbO_3$ thin films with different thicknesses. (a) SH0 frequencies, (b) SH0 K^2, (c) S0 frequencies, and (d) S0 K^2 at different wavelength.

does not exist because it mixes with the thickness-shear mode due to the large thickness/lateral wavelength ratio (h/λ). The electromechanical coupling K^2 is then calculated as [23]:

$$K^2 = f_o^2/f_s^2 - 1 \tag{1}$$

The results are plotted in Fig. 3 (b) and (d), showing high K^2 above 20%. The thicker $LiNbO_3$ shows lower K^2 in the small h/λ regime, agreeing with the previously reported SH0 [12] and S0 [11] dispersion.

Based on the above analysis, two key findings can be concluded for the proposed ADL-based acoustic loss study. First, the operating frequencies are determined mainly by λ. ADLs with the same λ but thicker $LiNbO_3$ operate at slightly higher frequencies. The thickness dependency is due to less mechanical and electrical loading of the Al electrodes in thicker films. Second, thanks to the high K^2 of SH0 and S0, low-loss and wideband ADLs are expected [49]. ADLs in thicker $LiNbO_3$ have slightly lower K^2, leading to worse directionality for the same design [49].

C. Acoustic Loss Extraction Method

The method is similar to the port extension de-embedding approach in microwave engineering. One example of the acoustic loss extraction approach will be showcased using SH0 ADLs in 400 nm X-cut $LiNbO_3$ with a cell length Λ of 3.2 μm and L_G between 100 and 600 μm. The simulated S-parameters will be conjugately matched. The propagation loss and group velocity of SH0 will be extracted from IL and group delay, respectively.

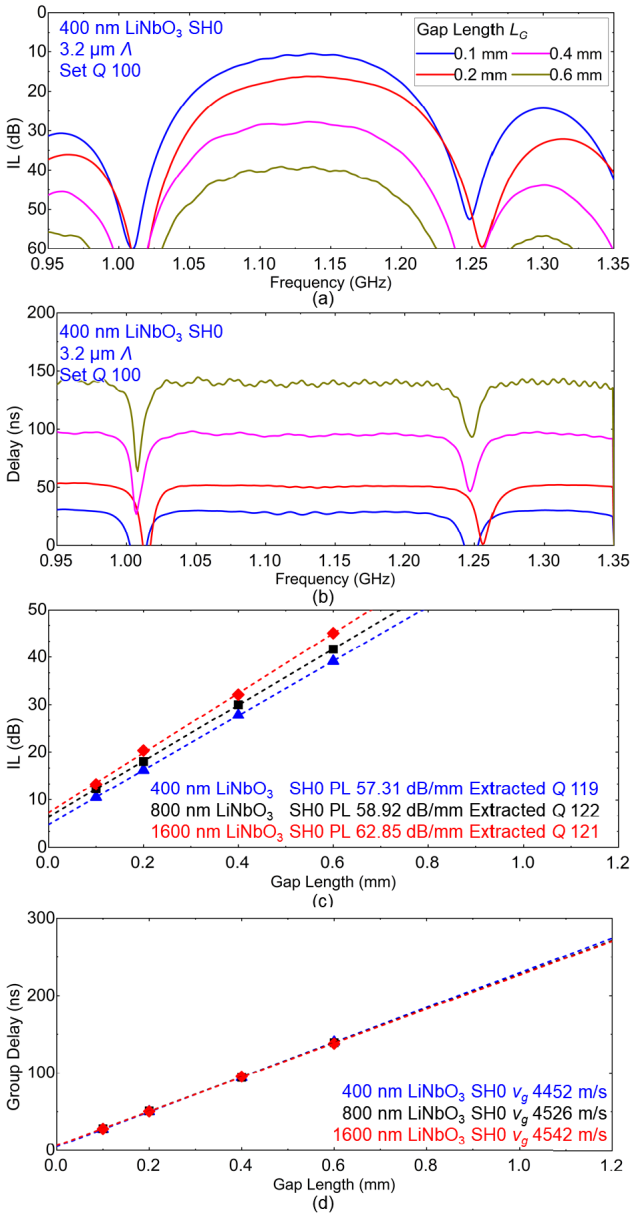

Fig. 4. Simulated (a) IL and (b) group delay of SH0 ADLs with 3.2 μm Λ in 400 nm $LiNbO_3$ with L_G between 0.1 and 0.6 mm (Q set as 100). Extracted (c) IL and (d) group delay for ADLs with different L_G and $LiNbO_3$ thickness.

The frequency-domain 3D FEA [Fig. 2 (c)] is set up following the procedure in [11]. Top and bottom surfaces are set as electrically open and mechanically free. Perfectly matched layers (PMLs) are applied to the longitudinal ends, emulating the energy dissipation into the substrate. A mechanical Q of the $LiNbO_3$ waveguide is set as 100 (defining imaginary loss modulus to the stiffness constants [51], [52]). The set mechanical Q will be compared with the extracted Q to validate the proposed method. Note that the set Q of 100 is significantly higher than that reported in prior experiments [12] to illustrate the loss extraction process. The S-parameters of the two-port devices are then obtained and conjugately matched for damping extraction.

The simulated IL and delay are plotted in Fig. 4 (a) and (b), respectively. The SH0 ADL shows a passband centered

at 1.12 GHz. Devices with longer L_G have higher IL and longer delays due to wave propagation and attenuation.

IL of ADLs with different L_G are extracted and fitted with a linear regression model [Fig. 4 (c)]. The 400 nm $LiNbO_3$ ADLs show a propagation loss (PL) of 57.31 dB/mm. Next, we can calculate the equivalent Q in the thin-film $LiNbO_3$ as [53]:

$$Q = \pi / PL \tag{2}$$

where the unit of PL is Np/λ. λ is the acoustic wavelength in the waveguide, slightly larger than the cell length Λ, because of the Al electrodes' electrical and mechanical loading effects. In this work, we use the eigenmode analysis (Section II-B) for λ. In this case, λ is 4.0 μm at f_o of 1.12 GHz. Thus, the PL can also be calculated as 0.23 dB/λ, or 0.0265 Np/λ. The equivalent propagation Q for 400 nm $LiNbO_3$ is 119, very close to the set material mechanical Q of 100. The difference is likely from the weak standing waves due to the transducers' finite unidirectionality [49]. The in-band group delay is also extracted and plotted against L_G in Fig. 4 (d). The group delay (v_g) is 4452 m/s.

Following a similar procedure, the IL and group delay of ADLs in 800 nm and 1600 nm $LiNbO_3$ are simulated and plotted in Fig. 4 (c) and (d). SH0 ADLs in 800 nm X-cut $LiNbO_3$ show passbands at 1.20 GHz, PL of 58.92 dB/mm (0.0225 dB/λ), extracted Q of 121, and v_g of 4526 m/s. SH0 ADLs in 1600 nm X-cut $LiNbO_3$ show passbands at 1.27 GHz, PL of 62.85 dB/mm (0.0224 dB/λ), extracted Q of 122, and v_g of 4542 m/s. ADLs in thicker $LiNbO_3$ films show higher IL and operating frequencies because of lower K^2 and higher f_s (Section II-B). The variation in v_g is caused by the in-band ripples from the finite directionality [49]. The extracted Qs match with the set value, validating the acoustic loss extraction approach.

The proposed ADL-based method will be used to experimentally characterize the acoustic loss in $LiNbO_3$ thin films for both S0 and SH0 waves. The loss in $LiNbO_3$ at different frequencies and with different thicknesses will be first compared to explore the attenuation origin in the current $LiNbO_3$ technologies. Next, the extracted values will be compared with the reported resonator Q to determine whether the acoustic resonator design or the thin-film $LiNbO_3$ is the dominant loss contributor.

III. Fabrication and Material Characterization

The devices are in-house fabricated using the fabrication process in [11]. $LiNbO_3$ wafers are first bonded to Si and then ground down to the desired thickness. To control the fabrication variation, the three samples are processed simultaneously after the thin-film transfer step.

The transferred $LiNbO_3$ thin films of different thicknesses are first characterized with X-ray powder diffraction (XRD) and atomic force microscopy (AFM). The XRD is measured with Bruker D8 advance XRD system. The rocking curves for the (110) plane are plotted in Fig. 5 (a) for the three thicknesses, respectively. The full width at half maximum (FWHM) of the three cases is 497, 397, and 270 arcsec, respectively. The thicker film shows significantly better quality, likely leading

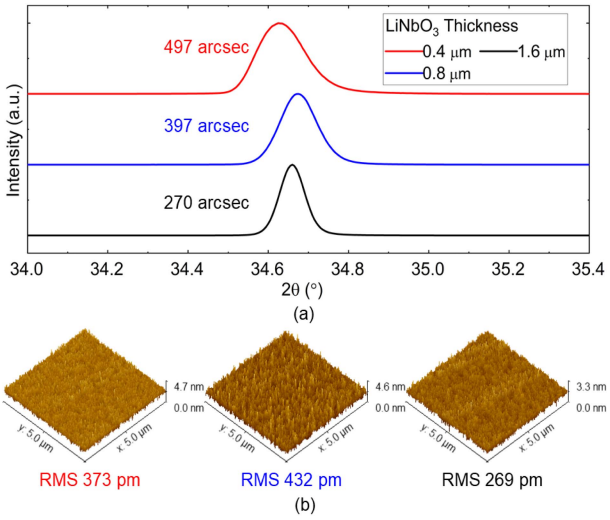

Fig. 5. (a) XRD rocking curve for (110) plane of thin-film $LiNbO_3$ and (b) AFM of the transfered $LiNbO_3$ thin films with 400, 800, and 1600 nm thickness.

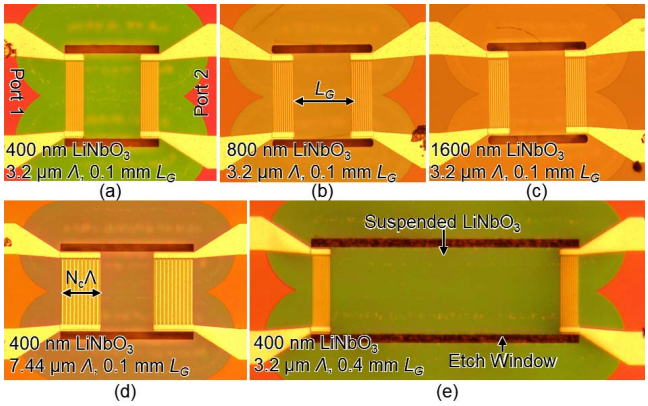

Fig. 6. Optical images of fabricated ADL testbeds. ADLs with 3.2 μm Λ and 0.1 mm L_G in (a) 400 nm, (b) 800 nm, and (c) 1600 nm X-cut $LiNbO_3$. (d) ADL with 7.44 μm Λ. (e) ADL with 0.4 mm L_G.

to lower IL. The AFM results are measured with Anton Paar Tosca 400, and plotted in Fig. 5 (b). The root mean square roughness (RMS) for the three cases are 373, 432, and 269 pm.

The optical images of fabricated ADL testbeds are shown in Fig. 6. Identical designs are placed in 400 [Fig. 6 (a)], 800 [Fig. 6 (b)], and 1600 nm [Fig. 6 (c)] X-cut $LiNbO_3$ thin films. Seven groups of ADLs with Λ between 3.2 [Fig. 6 (a)] and 7.44 μm [Fig. 6 (d)] are built, with Λ following a geometric sequence to space the passbands in the spectrum equally. Within each group, ADLs with L_G of 100 [Fig. 6 (a)], 200, 400 [Fig. 6 (e)], 600, 800 and 1200 μm are included. Two copies of devices are built, with the longitudinal direction of SH0 ADLs along $-10°$ to $+$Y axis and that of S0 ADLs along 30° to $+$Y axis for maximum K^2 and zero power flow angle [11].

IV. Measurements and Discussion

A. SH0 and S0 Mode ADL Testbed Examples

The fabricated ADLs are measured with a Keysight N5230A network analyzer at the -10 dBm power level in the air. In this section, we will present two example groups for SH0 and S0.

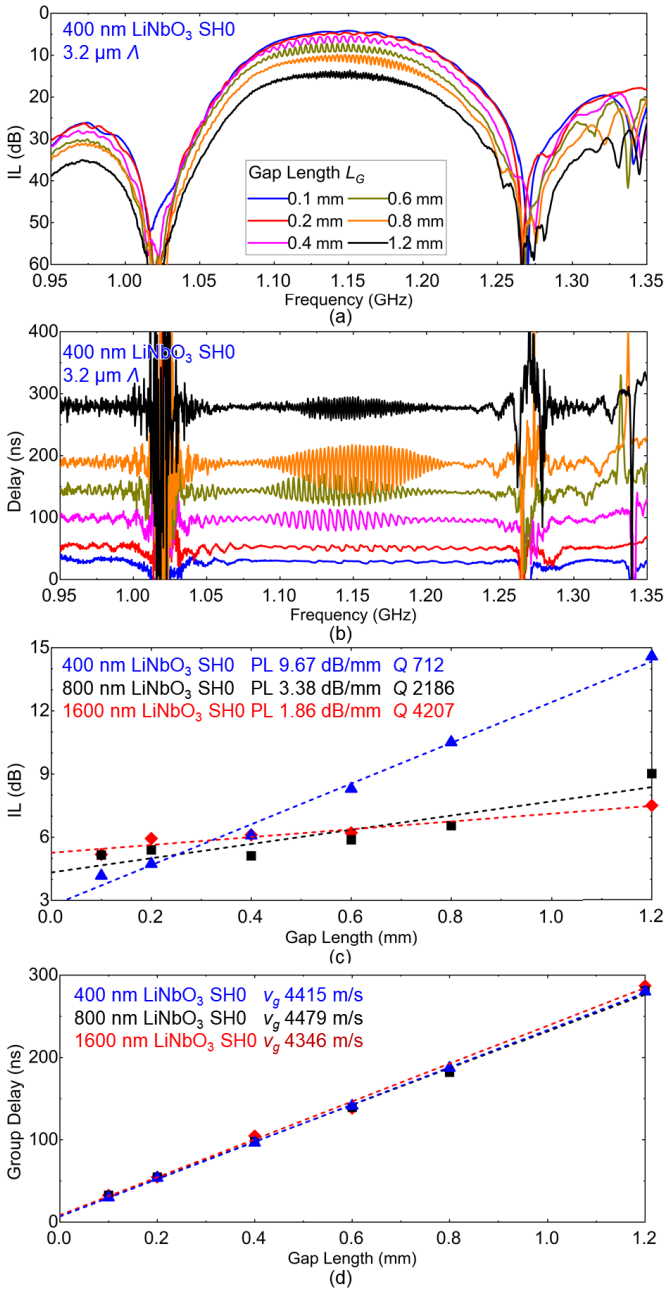

Fig. 7. Measured (a) IL and (b) group delay of SH0 ADLs with 3.2 μm Λ in 400 nm $LiNbO_3$ with L_G between 0.1 and 1.2 mm. Extracted (c) IL and (d) group delay for ADLs with different L_G and $LiNbO_3$ thickness.

The measured IL and group delay of SH0 ADLs in 400 nm X-cut $LiNbO_3$ (Λ of 3.2 μm and L_G between 100 and 1200 μm) are plotted in Fig. 7 (a) and (b). Passbands at 1.14 GHz are measured, matching well with the simulation in Section II-C. Longer ADLs show larger IL and delays from wave propagation and attenuation. The finite directionality in transducers causes the in-band ripples. IL of SH0 waves in 400 nm $LiNbO_3$ is plotted in Fig. 7 (c), showing PL of 9.67 dB/mm, an equivalent Q of 712. The group delay is plotted in Fig. 7 (d), showing v_g of 4415 m/s, matching the simulation.

Following the same procedure, the same SH0 ADL design in 800 and 1600 nm $LiNbO_3$ thin films are studied and plotted in Fig. 7 (c) and (d). ADLs in 800 nm $LiNbO_3$ are centered at 1.22 GHz, showing a PL of 3.38 dB/mm, an equivalent Q of 2186, and v_g of 4479 m/s. ADLs in 1600 nm $LiNbO_3$ are centered at 1.29 GHz, showing a PL of 1.86 dB/mm, an equivalent Q of 4207, and v_g of 4346 m/s. SH0 waves in the thinner films show larger acoustic attenuation.

Fig. 7 (c) also provides essential insights on attaining future low-loss ADL designs. Thinner films provide higher K^2 (Section II-B) for the same Λ, leading to better transducer directionality and lower transducer loss [49]. However, the thinner film has significantly higher PL (Fig. 7), unfavorable for longer delays. Therefore, an optimal $LiNbO_3$ thickness exists for ADLs with a desired delay design goal.

The measured IL and group delay of S0 ADLs in 400 nm X-cut $LiNbO_3$ (Λ of 6.4 μm and L_G between 100 and 1200 μm) are plotted in Fig. 8 (a) and (b). The passbands at 933 MHz are measured. A pronounced spurious mode (higher-order fundamental antisymmetric, A0) exists below the passband [11], causing interference in IL and group delay. IL of S0 waves in 400 nm $LiNbO_3$ is plotted in Fig. 8 (c), showing PL of 2.31 dB/mm, or an equivalent Q of 1518. The group delay is plotted in Fig. 8 (d), showing v_g of 6903 m/s. Compared to SH0, S0 waves are faster and less lossy, agreeing with prior reports [11], [12].

The same S0 ADL design in 800 and 1600 nm $LiNbO_3$ thin films are studied [Fig. 8 (c) and (d)]. ADLs in 800 nm $LiNbO_3$ are centered at 962 GHz, showing a PL of 1.47 dB/mm, an equivalent Q of 2451, and v_g of 7235 m/s. ADLs in 1600 nm $LiNbO_3$ are centered at 1.00 GHz, showing a PL of 0.80 dB/mm, an equivalent Q of 4645, and v_g of 7104 m/s. Similarly, S0 waves in the thinner films are much lossier.

B. Acoustic Loss in Thin-Film $LiNbO_3$

Following a similar analysis, 21 groups of SH0 ADLs and 16 groups of S0 ADLs with L_G between 100 and 1200 μm are measured and analyzed. Data from several S0 groups are missing (e.g., 400 nm $LiNbO_3$, Λ of 3.2 μm) when the highly dispersive A0 overtone overlaps with the S0 passband and generates large in-band ripples [11].

The key propagation characteristics, including frequencies, PL per wavelength, and PL per propagation time, are plotted in Fig. 9 (a) – (c) and Fig. 10 (a) – (c) for SH0 and S0. Each point represents the extracted slope from a group of 6 ADLs with the identical transducer but different gap lengths, mitigating the impact of fabrication variation to individual devices. Similar to the observations from the ADL examples in Section IV-A, ADLs in thicker $LiNbO_3$ tends to operate at slightly higher frequencies (lower K^2) and show lower PL than the same designs in thinner $LiNbO_3$. S0 devices show lower damping and operate at higher frequencies than SH0 counterparts.

Next, to quantitatively study the acoustic loss in thin-film $LiNbO_3$, the propagation Q is calculated using the FEA validated approach in Section II-C. The extracted Q for SH0 waves is plotted against the frequencies and thickness in Fig. 11 (a), each point from an ADL group. The values are listed in Table II. The plot show two remarkable findings. First, Q is mostly determined by the $LiNbO_3$ thickness, showing an

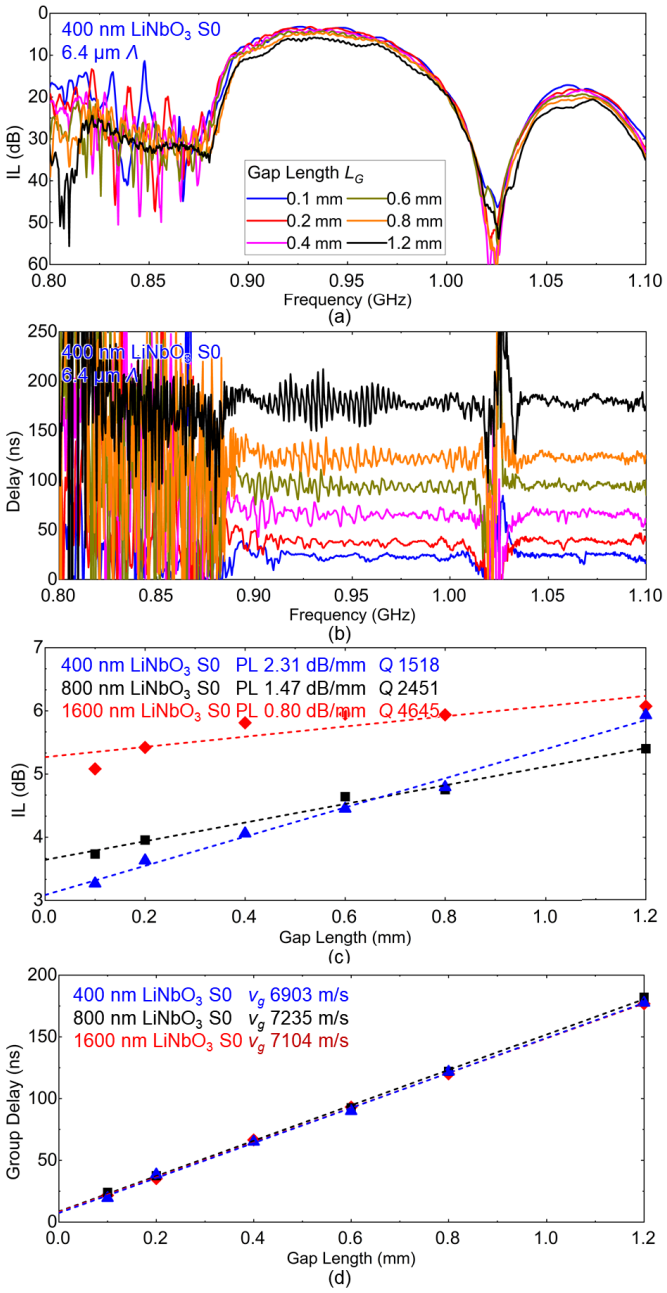

Fig. 8. Measured (a) IL and (b) group delay of S0 ADLs with 6.4 μm Λ in 400 nm $LiNbO_3$ with L_G between 0.1 and 1.2 mm. Extracted (c) IL and (d) group delay for ADLs with different L_G and $LiNbO_3$ thickness.

TABLE II
EXTRACTED Q OF SH0 IN AIR

	3.2 μm	3.68 μm	4.24 μm	4.88 μm	5.6 μm	6.4 μm	7.44 μm
400 nm	712	588	705	998	1067	1312	1997
800 nm	2186	1730	1492	2463	2056	2922	2571
1600 nm	4208	4407	4248	4282	5973	4393	3658

inverse relation between thickness and Q (1000 for 400 nm film, 2000 for 800 nm film, and 4000 for 1600 nm film). Such results suggest that likely the fabrication-induced surface

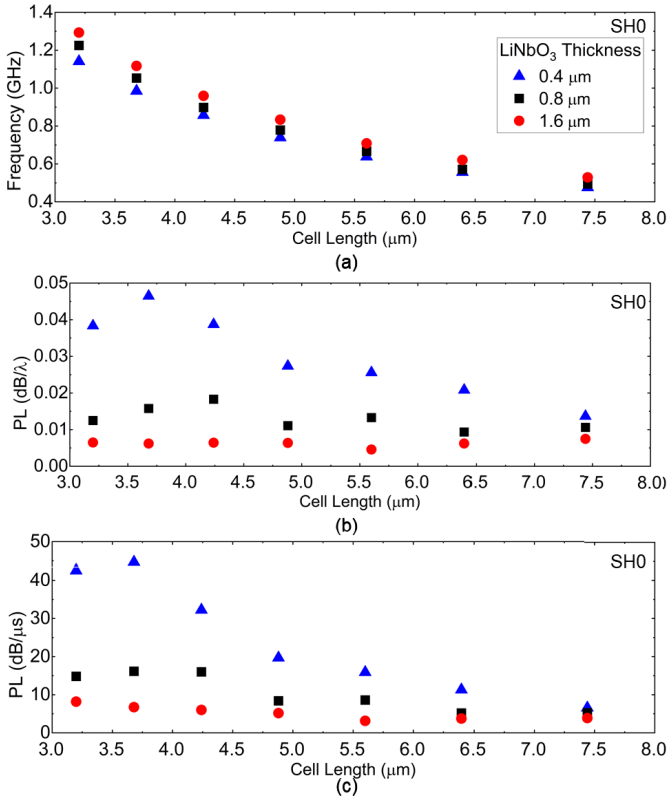

Fig. 9. Extracted propagation characteristics of SH0 waves in 400, 800, and 1600 nm X-cut $LiNbO_3$ thin films. (a) Center frequency, (b) PL per wavelength, and (c) PL per propagation time.

TABLE III
EXTRACTED Q OF S0 IN AIR

	3.2 μm	3.68 μm	4.24 μm	4.88 μm	5.6 μm	6.4 μm	7.44 μm
400 nm	1382	1378	1516	1578	--	1519	1897
800 nm	--	2053	2550	3215	2556	2451	2062
1600 nm	--	--	--	4168	5101	4646	6077

damage to the thin-film $LiNbO_3$ causes the PL exacerbation from that measured in bulk $LiNbO_3$ [28]. The damage is likely collectively contributed by the thin-film transfer and later dry etch process, as suggested by the material characterization in Section III. Second, lower frequency SH0 waves have slightly lower PL. This could be intuitively explained as SH0 waves with longer λ are less sensitive to the surface effects.

The extracted Q of S0 waves is plotted against the frequencies and thickness in Fig. 11 (b). The values are listed in Table III. Like the SH0 case, the $LiNbO_3$ thickness is the key determining factor of Q, and the S0 waves tend to be lossier at higher frequencies. The same argument is still valid that the crystal damage from the fabrication process might be the limiting factor in current thin-film $LiNbO_3$ acoustic platforms. Another interesting finding from comparing SH0 and S0 is that the S0 devices show higher Q than SH0 devices at the same frequency, likely due to the better tolerance to surface contamination thanks to the longer acoustic wavelength.

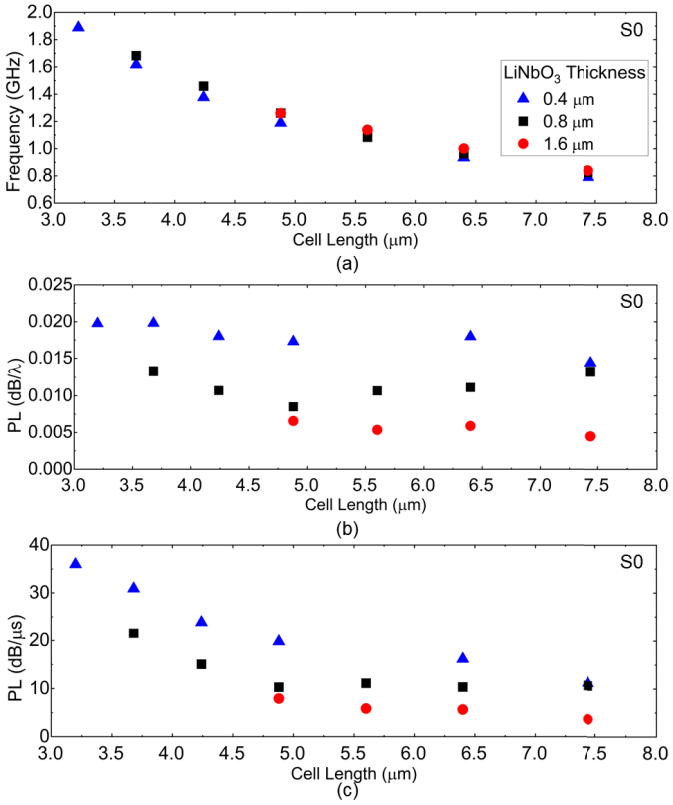

Fig. 10. Extracted propagation characteristics of S0 waves in 400, 800, and 1600 nm X-cut $LiNbO_3$ thin films. (a) Center frequency, (b) PL per wavelength, and (c) PL per propagation time.

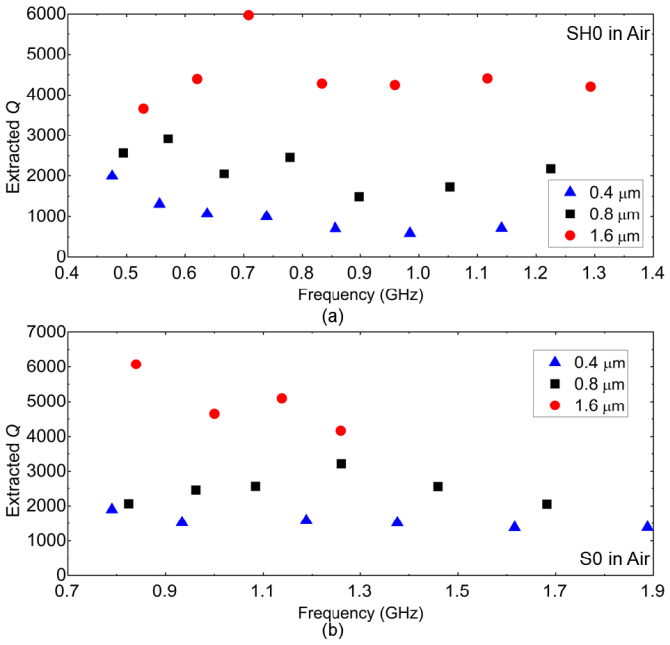

Fig. 11. Extracted Q in air of (a) SH0 and (b) S0 waves in thin-film $LiNbO_3$ of 400, 800, and 1600 nm thickness at different frequencies.

C. Effects of Air Damping on Acoustic Loss

To capture the air damping effects, ADLs are measured in vacuum, following the same procedure. The extracted Q for SH0 in vacuum is plotted in Fig. 12 (a) and listed

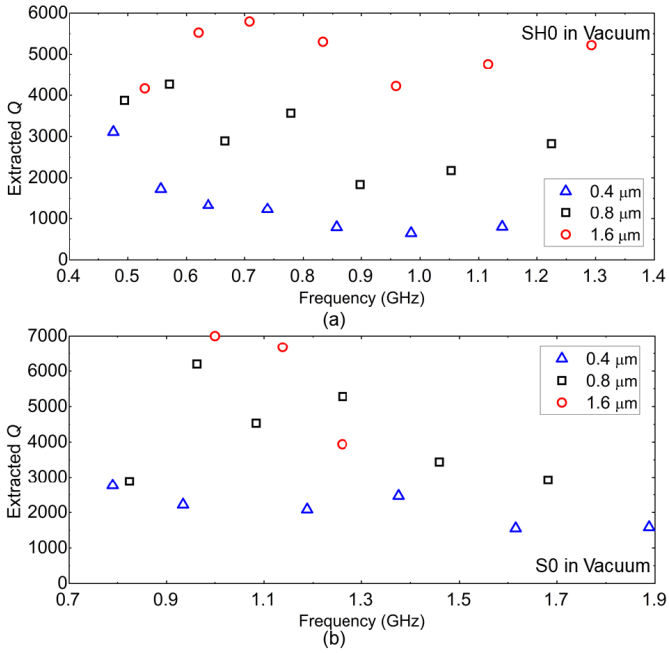

Fig. 12. Extracted Q in vacuum of (a) SH0 and (b) S0 waves in thin-film $LiNbO_3$ of 400, 800, and 1600 nm thickness at different frequencies.

TABLE IV
EXTRACTED Q OF SH0 IN VACUUM

	3.2 μm	3.68 μm	4.24 μm	4.88 μm	5.6 μm	6.4 μm	7.44 μm
400 nm	801	646	791	1230	1328	1730	3109
800 nm	2826	2176	1837	3564	2891	4265	3873
1600 nm	5225	4761	4221	5308	5798	5527	4165

TABLE V
EXTRACTED Q OF S0 IN VACUUM

	3.2 μm	3.68 μm	4.24 μm	4.88 μm	5.6 μm	6.4 μm	7.44 μm
400 nm	1582	1551	2463	2080	--	2219	2766
800 nm	--	2922	3437	5279	4530	6197	2883
1600 nm	--	--	--	3939	6676	7000	8073

in Table IV. Compared to those in air, the extracted Q show around X1.5 enhancement, agreeing with the reported Q enhancement in resonator cases [54]. The S0 results are plotted in Fig. 12 (b) and listed in Table V. Similar amount of Q enhancement is observed.

One caveat in the current loss study is that the high Q above 5000 has limited accuracy in the S0 case. For S0 ADLs with such low PL, the difference in IL of devices with L_G of 100 and 1200 μm is less than 1 dB. The measurement error from the probe contact (in the order of 0.1 dB) can significantly affect the Q, as seen in Fig. 12. More accurate results for S0 waves will be studied in future works using ADLs with longer L_G.

D. Effects of Temperature on Acoustic Loss

The temperature dependency of acoustic loss will be studied by measuring PL at different temperatures in vacuum.

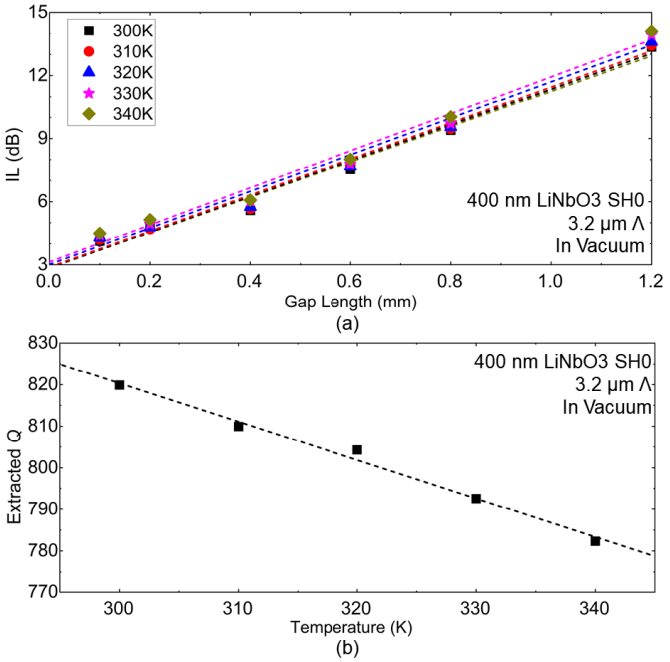

Fig. 13. (a) IL of SH0 ADLs at different temperature (3.2 μm Λ, 400 nm $LiNbO_3$, L_G between 0.1 and 1.2 mm). (b) Extracted temperature dependency of Q in vacuum.

Thin-film $LiNbO_3$ resonators have been reported to operate between 700 K [55] and 130 K [54]. A general trend is that the $LiNbO_3$ resonator tends to be lossier at higher temperatures, similar to other MEMS devices [30]. However, it is difficult to extract the effects of temperature on attenuation in thin-film $LiNbO_3$ from the resonator results since different loss mechanisms, e.g., anchor loss, have different temperature dependencies [29]. We will use the SH0 ADL examples in Section IV-A (400 nm X-cut $LiNbO_3$ with Λ of 3.2 μm and L_G between 100 and 1200 μm) to showcase the relation.

The extracted IL of different ADLs at temperatures between 300 and 340 K is plotted in Fig. 13 (a). ADLs tend to show higher IL at higher temperatures. To remove the transducer effects, the PL and Q are extracted using the linear regression approach and plotted in Fig. 13 (b). The equivalent Q drops from 820 to 780 at 340 K, showing higher acoustic attenuation in $LiNbO_3$ thin-films at higher temperatures, agreeing with the trend reported earlier in resonators [56]. The origin for the Q degradation will be identified in future works.

E. Discussion and Future Work

The measured Q in air and vacuum from ADL results can be compared with the reported Q of resonators at similar frequencies and with similar stack thickness. As expected earlier, the extracted Q in thin-film $LiNbO_3$ is much higher than that reported in the resonators because we eliminate the effects from anchor loss and electrode-induced electrical and mechanical loading. Such results point out design space in further optimizing resonator configuration and enhancing electrode quality for higher-Q thin-film $LiNbO_3$ resonators.

However, it is important to note that the PL (or Q) reported in this work is not the absolute upper limit in thin-film $LiNbO_3$ technologies but the typical values from current fabrication processes. It is possible to further mitigate loss by reducing degradation of $LiNbO_3$ during the thin-film transfer and later etching steps, and potentially including the annealing process [21]. We still have a long way to go before approaching the ultra-low acoustic damping in bulk $LiNbO_3$ [28].

The following aspects could be further investigated in future works. First, theoretical work is required to understand better the experimental data reported in this work, especially to establish the relation between the material quality and propagation loss. Second, acoustic loss is only studied in the orientations with the maximum K^2 to eliminate diffraction resulting from non-zero power flow angles at other orientations [57]. It would be interesting to study the damping in other orientations and potentially establish the correlation between PL and K^2 (causal or otherwise). Third, higher-order modes in the thickness directions [58], e.g., A1, whose frequencies are determined mainly by the stack thickness, need to be studied in future works. The current bottleneck is to build higher-order mode ADLs in different thickness $LiNbO_3$, while still maintaining the same operating frequency. Fourth, the acoustic loss in other structures, e.g., electrodes and metalized piezoelectric thin films, could be studied by placing them in the acoustic waveguide. Finally, future work on deciphering the origins of PL for S0 and SH0 using the experimental data is of great value.

Finally, the loss extraction framework based on unidirectional ADLs is readily extendable to other thin-film structures, such as the emerging high-quality ScAlN/AlN piezoelectric thin films [59]–[64], by using the reported AlN unidirectional ADL designs [65]. Thus, this reported acoustic loss analysis approach could facilitate the future development of thin-film low-loss wideband microsystems in various acoustic platforms.

V. Conclusion

In this work, we experimentally extract the acoustic loss in thin-film $LiNbO_3$ using ADL testbeds. Acoustic attenuation of S0 and SH0 waves are systematically studied in X-cut $LiNbO_3$ of different thicknesses. Acoustic loss in thinner $LiNbO_3$ is found significantly higher, suggesting the fabrication-related crystal degradation is likely the limiting factor. The extracted Q limits of thin-film $LiNbO_3$ are higher than those in prior resonators, pointing to optimization opportunities for resonator configuration and electrode quality. The proposed ADL-based loss extraction framework is readily extendable to other acoustic thin-film structures.

References

[1] M. Kadota, T. Ogami, K. Yamamoto, and H. Tochishita, "$LiNbO_3$ thin film for A_1 mode of Lamb wave resonators," *Phys. Status Solidi Appl. Mater. Sci.*, vol. 208, no. 5, pp. 1068–1071, May 2011.

[2] R. H. Olsson *et al.*, "A high electromechanical coupling coefficient SH0 Lamb wave lithium niobate micromechanical resonator and a method for fabrication," *Sens. Actuators A, Phys.*, vol. 209, pp. 183–190, Mar. 2014.

[3] V. Plessky, S. Yandrapalli, P. J. Turner, L. G. Villanueva, J. Koskela, and R. B. Hammond, "5 GHz laterally-excited bulk-wave resonators (XBARs) based on thin platelets of lithium niobate," *Electron. Lett.*, vol. 55, no. 2, pp. 98–100, Jan. 2019.

[4] R. Wang, S. A. Bhave, and K. Bhattacharjee, "Design and fabrication of S_0 Lamb-wave thin-film lithium niobate micromechanical resonators," *J. Microelectromech. Syst.*, vol. 24, no. 2, pp. 300–308, Apr. 2015.

[5] M. Faizan and L. G. Villanueva, "Frequency-scalable fabrication process flow for lithium niobate based Lamb wave resonators," *J. Micromech. Microeng.*, vol. 30, no. 1, 2019, Art. no. 15008.

[6] S. Gong and G. Piazza, "Design and analysis of lithium–niobate-based high electromechanical coupling RF-MEMS resonators for wideband filtering," *IEEE Trans. Microw. Theory Techn.*, vol. 61, no. 1, pp. 403–414, Jan. 2013.

[7] T. Manzaneque, R. Lu, Y. Yang, and S. Gong, "A high FoM lithium niobate resonant transformer for passive voltage amplification," in *Proc. Solid-State Sensors, Actuat. Microsyst.*, 2017, pp. 798–801.

[8] G. Vidal-Alvarez, M. Figura, A. Kochhar, L. Colombo, and G. Piazza, "Voltage amplification of radio frequency signals with pitch-asymmetric acoustic delay lines," *J. Microelectromech. Syst.*, vol. 29, no. 2, pp. 236–247, Apr. 2020.

[9] L. Colombo, A. Kochhar, G. Vidal-Alvarez, and G. Piazza, "High-figure-of-merit X-cut lithium niobate MEMS resonators operating around 50 MHz for large passive voltage amplification in radio frequency applications," *IEEE Trans. Ultrason., Ferroelectr., Freq. Control*, vol. 67, no. 7, pp. 1392–1402, Jul. 2020.

[10] T. Manzaneque, R. Lu, Y. Yang, and S. Gong, "Low-loss and wideband acoustic delay lines," *IEEE Trans. Microw. Theory Techn.*, vol. 67, no. 4, pp. 1379–1391, Apr. 2019.

[11] R. Lu, T. Manzaneque, Y. Yang, M.-H. Li, and S. Gong, "Gigahertz low-loss and wideband s0 mode lithium niobate acoustic delay lines," *IEEE Trans. Ultrason., Ferroelectr., Freq. Control*, vol. 66, no. 8, pp. 1373–1386, Aug. 2019.

[12] R. Lu, Y. Yang, M.-H. Li, T. Manzaneque, and S. Gong, "GHz broadband SH0 mode lithium niobate acoustic delay lines," *IEEE Trans. Ultrason., Ferroelectr., Freq. Control*, vol. 67, no. 2, pp. 402–412, Feb. 2020.

[13] R. Lu, Y. Yang, S. Link, and S. Gong, "Low-loss 5-GHz first-order antisymmetric mode acoustic delay lines in thin-film lithium niobate," *IEEE Trans. Microw. Theory Techn.*, vol. 69, no. 1, pp. 541–550, Jan. 2021.

[14] R. Lu, T. Manzaneque, Y. Yang, and S. Gong, "S0-mode lithium niobate acoustic delay lines with 1 dB insertion loss," in *Proc. IEEE Int. Ultrason. Symp.*, Oct. 2018, pp. 1–9.

[15] H. Mansoorzare and R. Abdolvand, "Acoustoelectric non-reciprocity in lithium niobate-on-silicon delay lines," *IEEE Electron Device Lett.*, vol. 41, no. 9, pp. 1444–1447, Sep. 2020.

[16] R. Lu, T. Manzaneque, Y. Yang, L. Gao, A. Gao, and S. Gong, "A radio frequency nonreciprocal network based on switched acoustic delay lines," *IEEE Trans. Microw. Theory Techn.*, vol. 67, no. 4, pp. 1516–1530, Apr. 2019.

[17] S. Ghosh and M. Ricci, "A 3-port circulator based on non-reciprocal acoustoelectric delay lines," in *IEEE Int. Freq. Control Symp.*, Jul. 2020, pp. 1–3.

[18] L. Shao *et al.*, "Integrated lithium niobate acousto-optic frequency shifter," in *Proc. Conf. Lasers Electro-Opt.*, 2020, pp. 23728–23738.

[19] L. Shao *et al.*, "Microwave-to-optical conversion using lithium niobate thin-film acoustic resonators," *Optica*, vol. 6, no. 12, pp. 1498–1505, 2019.

[20] L. Cai *et al.*, "Acousto-optical modulation of thin film lithium niobate waveguide devices," *Photon. Res.*, vol. 7, no. 9, p. 1003, 2019.

[21] L. Cai, A. Mahmoud, and G. Piazza, "Low-loss waveguides on Y-cut thin film lithium niobate: Towards acousto-optic applications," *Opt. Exp.*, vol. 27, no. 7, pp. 9794–9802, 2019.

[22] W. Jiang *et al.*, "Lithium niobate piezo-optomechanical crystals," *Optica*, vol. 6, no. 7, pp. 845–853, 2019.

[23] K. Hashimoto, *Surface Acoustic Wave Devices in Telecommunications*. Berlin, Germany: Springer, 2000.

[24] M. Pijolat *et al.*, "Large QXF product for HBAR using smart Cut transfer of $LiNbO_3$ thin layers onto $LiNbO_3$ substrate," in *Proc. IEEE Int. Ultrason. Symp.*, Jan. 2008, pp. 201–204.

[25] E. Butaud *et al.*, "Smart Cut Piezo On Insulator (POI) substrates for high performances SAW components," in *Proc. IEEE Int. Ultrason. Symp. (IUS)*, Sep. 2020, pp. 1–4.

[26] R. Lu, M. Breen, A. E. Hassanien, Y. Yang, and S. Gong, "A piezoelectric micromachined ultrasonic transducer using thin-film lithium niobate," *J. Microelectromech. Syst.*, vol. 29, no. 6, pp. 1412–1414, Dec. 2020.

[27] Y. Yang, R. Lu, L. Gao, and S. Gong, "10–60-GHz electromechanical resonators using thin-film lithium niobate," *IEEE Trans. Microw. Theory Techn.*, vol. 68, no. 12, pp. 5211–5220, Dec. 2020.

[28] I. L. Bajak, A. McNab, J. Richter, and C. D. W. Wilkinson, "Attenuation of acoustic waves in lithium niobate," *J. Acoust. Soc. Amer.*, vol. 69, no. 3, pp. 689–695, Mar. 1981.

[29] J. Segovia-fernandez *et al.*, "Anchor losses in AlN contour mode resonators," *J. Microelectromech. Syst.*, vol. 24, no. 2, pp. 1–11, Apr. 2014.

[30] B. Kim *et al.*, "Temperature dependence of quality factor in MEMS resonators," *J. Microelectromech. Syst.*, vol. 17, no. 3, pp. 755–766, Jun. 2008.

[31] S. Ghaffari *et al.*, "Accurate modeling of quality factor behavior of complex silicon MEMS resonators," *J. Microelectromech. Syst.*, vol. 24, no. 2, pp. 276–288, Apr. 2015.

[32] R. H. Olsson *et al.*, "Lamb wave micromechanical resonators formed in thin plates of lithium niobate," in *Proc. Solid-State Sensor, Actuator, Microsyst. Workshop*, 2014, pp. 281–284.

[33] Y.-H. Song and S. Gong, "Spurious mode suppression in SH0 lithium niobate laterally vibrating MEMS resonators," in *IEDM Tech. Dig.*, Dec. 2015, pp. 15–18.

[34] S. Gong and G. Piazza, "Overmoded shear horizontal wave MEMS resonators using X-cut lithium niobate thin film," in *Proc. IEEE Int. Ultrason. Symp.*, Sep. 2014, pp. 568–571.

[35] A. Kochhar, A. Mahmoud, Y. Shen, N. Turumella, and G. Piazza, "X-cut lithium niobate-based shear horizontal resonators for radio frequency applications," *J. Microelectromech. Syst.*, vol. 29, no. 6, pp. 1464–1472, Dec. 2020.

[36] M. Kadota, Y. Kuratani, T. Kimura, M. Esashi, and S. Tanaka, "Ultra-wideband and high frequency resonators using shear horizontal type plate wave in $LiNbO_3$ thin plate," *Jpn. J. Appl. Phys.*, vol. 53, no. 7, 2014, Art. no. 07KD03.

[37] C.-Y. Chen, S.-S. Li, M.-H. Li, A. Gao, R. Lu, and S. Gong, "Q-enhanced lithium niobate SH0 resonators with optimized acoustic boundaries," in *Proc. IEEE Int. Freq. Control Symp. Eur. Freq. Time Forum*, Apr. 2019, pp. 1–4.

[38] R. Lu, T. Manzaneque, Y. Yang, and S. Gong, "Exploiting parallelism in resonators for large voltage gain in low power wake up radio front ends," in *Proc. IEEE Micro Electro Mech. Syst. (MEMS)*, Jan. 2018, pp. 747–750.

[39] S. Gong and G. Piazza, "Figure-of-merit enhancement for laterally vibrating lithium niobate mems resonators," *IEEE Trans. Electron Devices*, vol. 60, no. 11, pp. 3888–3894, Oct. 2013.

[40] L. Colombo, A. Kochhar, G. Vidal-Alvarez, and G. Piazza, "X-cut lithium niobate laterally vibrating Mems resonator with figure of merit of 1560," *J. Microelectromech. Syst.*, vol. 27, no. 4, pp. 602–604, Aug. 2018.

[41] L. Colombo, A. Kochhar, G. Vidal-Alvarez, and G. Piazza, "Impact of frequency mismatch on the quality factor of large arrays of X-cut lithium niobate MEMS resonators," *J. Microelectromech. Syst.*, vol. 29, no. 6, pp. 1455–1463, Dec. 2020.

[42] R. Lu, Y. Yang, S. Link, and S. Gong, "A1 resonators in 128° Y-cut lithium niobate with electromechanical coupling of 46.4%," *J. Microelectromech. Syst.*, vol. 29, no. 3, pp. 313–319, 2020.

[43] Y. Yang, R. Lu, and S. Gong, "High q antisymmetric mode lithium niobate MEMS resonators with spurious mitigation," *J. Microelectromech. Syst.*, vol. 29, no. 2, pp. 135–143, Apr. 2020.

[44] Y. Yang, L. Gao, R. Lu, and S. Gong, "Lateral spurious mode suppression in lithium niobate A1 resonators," *IEEE Trans. Ultrason., Ferroelectr., Freq. Control*, vol. 68, no. 5, pp. 1930–1937, May 2021.

[45] M. Bousquet *et al.*, "Single-mode high frequency $LiNbO_3$ film bulk acoustic resonator," in *Proc. IEEE Int. Ultrason. Symp. (IUS)*, Oct. 2019, pp. 84–87.

[46] Y. Yang, R. Lu, and S. Gong, "A 1.65 GHz lithium niobate A1 resonator with electromechanical coupling of 14% and Q of 3112," in *Proc. IEEE 32nd Int. Conf. Micro Electro Mech. Syst. (MEMS)*, Jan. 2019, pp. 875–878.

[47] M. Bousquet *et al.*, "Lithium niobate film bulk acoustic wave resonator for sub-6 GHz filters," in *Proc. IEEE Int. Ultrason. Symp. (IUS)*, Sep. 2020, pp. 1–4.
[48] T. Kimura, M. Omura, Y. Kishimoto, and K. Hashimoto, "Comparative study of acoustic wave devices using thin piezoelectric plates in the 3–5-GHz range," *IEEE Trans. Microw. Theory Techn.*, vol. 67, no. 3, pp. 915–921, Mar. 2019.
[49] C. S. Hartmann and B. P. Abbott, "Overview of design challenges for single phase unidirectional SAW filters," in *Proc. IEEE Int. Ultrason. Symp.*, Apr. 1989, pp. 79–89.
[50] I. E. Kuznetsova, B. D. Zaitsev, S. G. Joshi, and I. A. Borodina, "Investigation of acoustic waves in thin plates of lithium niobate and lithium tantalate," *IEEE Trans. Ultrason., Ferroelectr., Freq. Control*, vol. 48, no. 1, pp. 322–328, Jan. 2001.
[51] A. K. Chopra, *Dynamics of Structures*. London, U.K.: Pearson, 2007.
[52] *Structural Mechanics Module User's Guide*, COMSOL, Stockholm, Sweden, 2012.
[53] W. M. Siebert, *Circuits, Signals, and Systems*. Cambridge, MA, USA: MIT Press, 1986.
[54] L. Colombo, A. Kochhar, G. Vidal-Alvarez, and G. Piazza, "Investigations on the quality factor of lithium niobate laterally vibrating resonators with figure of merit greater than 1,500," in *Proc. IEEE Int. Ultrason. Symp. (IUS)*, Oct. 2018, pp. 1–4.
[55] S. R. Eisner, C. A. Chapin, R. Lu, Y. Yang, S. Gong, and D. G. Senesky, "A laterally vibrating lithium niobate MEMS resonator array operating at 500°C in air," *Sensors*, vol. 21, no. 1, pp. 1–9, 2020.
[56] M.-H. Li, C.-Y. Chen, R. Lu, Y. Yang, T. Wu, and S. Gong, "Power-efficient ovenized lithium niobate SH0 resonator arrays with passive temperature compensation," in *Proc. IEEE 32nd Int. Conf. Micro Electro Mech. Syst. (MEMS)*, Jan. 2019, pp. 911–914.
[57] I. E. Kuznetsova, B. D. Zaitsev, A. A. Teplykh, S. G. Joshi, and A. S. Kuznetsova, "The power flow angle of acoustic waves in thin piezoelectric plates," *IEEE Trans. Ultrason., Ferroelectr., Freq. Control*, vol. 55, no. 9, pp. 1984–1991, Sep. 2008.
[58] R. Lu, Y. Yang, S. Link, and S. Gong, "Enabling higher order Lamb wave acoustic devices with complementarily oriented piezoelectric thin films," *J. Microelectromech. Syst.*, vol. 29, no. 5, pp. 1332–1346, Oct. 2020.
[59] M. Park, Z. Hao, R. Dargis, A. Clark, and A. Ansari, "Epitaxial aluminum scandium nitride super high frequency acoustic resonators," *J. Microelectromech. Syst.*, vol. 29, no. 4, pp. 490–498, Aug. 2020.
[60] S. Kinoshita and T. Yanagitani, "GHz BAW piezoelectric transformers with high voltage gain using the combination of high and low dielectric constant thin films," in *Proc. IEEE Int. Ultrason. Symp. (IUS)*, Sep. 2020, pp. 1–4.
[61] C. Moe *et al.*, "Highly doped AlScN 3.5 GHz XBAW resonators with 16% k2eff for 5G RF filter applications," in *Proc. IEEE Int. Ultrason. Symp. (IUS)*, Sep. 2020, pp. 1–4.
[62] M. Assylbekova, G. Chen, G. Michetti, M. Pirro, L. Colombo, and M. Rinaldi, "11 GHz lateral-field-excited aluminum nitride cross-sectional Lamé mode resonator," in *Proc. Joint Conf. IEEE Int. Freq. Control Symp. Int. Symp. Appl. Ferroelectr. (IFCS-ISAF)*, Jul. 2020, pp. 1–4.
[63] L. Colombo, A. Kochhar, C. Xu, G. Piazza, S. Mishin, and Y. Oshmyansky, "Investigation of 20% scandium-doped aluminum nitride films for MEMS laterally vibrating resonators," in *Proc. IEEE Int. Ultrason. Symp.*, May 2017, pp. 1–4.
[64] G. Esteves *et al.*, "$Al_{0.68}Sc_{0.32}N$ Lamb wave resonators with electromechanical coupling coefficients near 10.28%," *Appl. Phys. Lett.*, vol. 118, no. 17, Apr. 2021, Art. no. 171902.
[65] R. Lu, S. Link, and S. Gong, "A unidirectional transducer design for scaling GHz AlN-based RF microsystems" *IEEE Trans. Ultrason., Ferroelectr., Freq. Control*, vol. 67, no. 6, pp. 1250–1257, Jun. 2020.

Ruochen Lu (Member, IEEE) received the B.E. degree (Hons.) in microelectronics from Tsinghua University, Beijing, China, in 2014, and the M.S. and Ph.D. degrees in electrical engineering from the University of Illinois at Urbana-Champaign (UIUC), Urbana, IL, USA, in 2017 and 2019, respectively. He is currently an Assistant Professor with the Department of Electrical and Computer Engineering, The University of Texas at Austin. His works aim to demonstrate reconfigurable and tunable RF functions using novel MEMS platforms, toward higher operating frequencies and more efficient transduction between the EM and acoustic domains. He also works on ultrasonic transducers and multi-physics hybrid microsystems for signal processing, sensing, and computing applications. His research primarily focuses on developing chip-scale acoustic and electromagnetic components, and microsystems for RF applications. He received the Best Student Paper Award at the 2017 IEEE International Frequency Control Symposium and the 2018 IEEE International Ultrasonics Symposium.

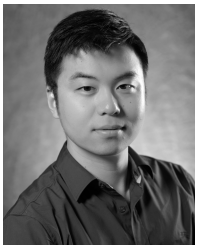

Yansong Yang (Member, IEEE) received the B.S. degree in electrical and electronic engineering from the Huazhong University of Science and Technology, Wuhan, China, in 2014, and the M.S. and Ph.D. degrees in electrical engineering from the University of Illinois at Urbana-Champaign, Urbana, IL, USA, in 2017 and 2019, respectively. He is currently a Post-Doctoral Researcher with the University of Illinois at Urbana-Champaign. His research interests include design and microfabrication techniques of RF MEMS resonators, filters, switches, and photonic integrated circuits. He has won the Second Place in Best Paper Competition at the 2018 IEEE International Microwave Symposium and the Best Paper Award at the 2019 IEEE International Ultrasonics Symposium. He was also a Finalist of the Best Paper Award at the 2018 IEEE International Frequency Control Symposium and the Advanced Practices Paper Competition Award at the 2020 IEEE International Microwave Symposium. He was also a recipient of the 2019 P. D. Coleman Graduate Research Award from the Department of Electrical and Computer Engineering, UIUC.

Songbin Gong (Senior Member, IEEE) received the Ph.D. degree in electrical engineering from the University of Virginia, Charlottesville, VA, USA, in 2010. He is currently an Associate Professor and the Intel Alumni Fellow with the Department of Electrical and Computer Engineering and the Micro and Nanotechnology Laboratory, University of Illinois at Urbana-Champaign, Urbana, IL, USA. His research primarily focuses on design and implementation of radio frequency microsystems, components, and subsystems for reconfigurable RF front ends. In addition, his research explores hybrid microsystems based on the integration of MEMS devices with photonics or circuits for signal processing and sensing. He is a Technical Committee Member of the IEEE International Microwave Symposium, the International Frequency Control Symposium, and the International Ultrasonic Symposium. He was a recipient of the 2014 Defense Advanced Research Projects Agency Young Faculty Award, the 2017 NASA Early Career Faculty Award, the 2019 UIUC College of Engineer Dean's Award for Excellence in Research, and the 2019 Ultrasonics Early Career Investigator Award. Along with his students and postdoctoral researchers, he received the Best Paper Award from the 2017 and 2019 IEEE International Frequency Control Symposium; the 2018, 2019, and 2020 International Ultrasonics Symposium; and won the Second and Third Place in Best Paper Competition at the 2018 and 2020 IEEE International Microwave Symposium. He also serves as the Chair for MTT TC6, and an Associate Editor for IEEE TRANSACTIONS ON ULTRASONICS, FERROELECTRICS, AND FREQUENCY CONTROL, JOURNAL OF MICROELECTROMECHANICAL SYSTEMS, and JMW.